catalysts

MDPI

Article

Defect Engineering and Surface Polarization of TiO_2 Nanorod Arrays toward Efficient Photoelectrochemical Oxygen Evolution

Yueying Li [1,*,†], Shiyu Liang [2,†], Huanhuan Sun [2], Wei Hua [2] and Jian-Gan Wang [2,*]

[1] New Energy (Photovoltaic) Industry Research Center, Qinghai University, No. 251, Ningda Road, Xi'ning 810016, China
[2] State Key Laboratory of Solidification Processing, Center for Nano Energy Materials, School of Materials Science and Engineering, Northwestern Polytechnical University and Shaanxi Joint Lab of Graphene (NPU), No. 127, Youyi West Road, Xi'an 710072, China
* Correspondence: liyueying0729@163.com (Y.L.); wangjiangan@nwpu.edu.cn (J.-G.W.)
† These authors contributed equally to this work.

Abstract: The relatively low photo-conversion efficiencies of semiconductors greatly restrict their real-world practices toward photoelectrochemical water splitting. In this work, we demonstrate the fabrication of TiO_{2-x} nanorod arrays enriched with oxygen defects and surface-polarized hydroxyl groups by a facile surface reduction method. The oxygen defects located in the bulk/surface of TiO_{2-x} enable fast charge transport and act as catalytically active sites to accelerate the water oxidation kinetics. Meanwhile, the hydroxyl groups could establish a surface electric field by polarization, for efficient charge separation. The as-optimized TiO_{2-x} nanorod photoanode achieves a high photocurrent density of 2.62 mA cm^{-2} without any cocatalyst loading at 1.23 V_{RHE} under 100 mW cm^{-2}, which is almost double that of the bare TiO_2 counterpart. Notably, the surface charge separation and injection efficiency of the TiO_{2-x} photoanode reach as high as 80% and 97% at 1.23 V_{RHE}, respectively, and the maximum incident photon-to-current efficiency reaches 90% at 400 nm. This work provides a new surface treatment strategy for the development of high-performance photoanodes in photoelectrochemical water splitting.

Keywords: titanium dioxide; defect engineering; surface polarization; photoelectrochemical water splitting

check for updates

Citation: Li, Y.; Liang, S.; Sun, H.; Hua, W.; Wang, J.-G. Defect Engineering and Surface Polarization of TiO_2 Nanorod Arrays toward Efficient Photoelectrochemical Oxygen Evolution. *Catalysts* **2022**, *12*, 1021. https://doi.org/10.3390/catal12091021

Academic Editor: Simonetta Palmas

Received: 18 August 2022
Accepted: 6 September 2022
Published: 8 September 2022

Publisher's Note: MDPI stays neutral with regard to jurisdictional claims in published maps and institutional affiliations.

Copyright: © 2022 by the authors. Licensee MDPI, Basel, Switzerland. This article is an open access article distributed under the terms and conditions of the Creative Commons Attribution (CC BY) license (https://creativecommons.org/licenses/by/4.0/).

1. Introduction

Solar-driven photoelectrochemical (PEC) water splitting, a sustainable strategy to generate clean hydrogen fuels, is deemed a major breakthrough to alleviate the current energy crisis and environmental deterioration [1–5]. Recently, various semiconductor photoelectrodes, such as TiO_2, Fe_2O_3, $BiVO_4$, and WO_3, have attracted extensive attention to enhance the PEC performance. In particular, TiO_2 is still regarded as a benchmark photocatalyst thanks to its low cost, appropriate energy band structure, and excellent chemical stability [6,7]. However, the PEC water splitting performance of TiO_2 is severely limited by its poor light utilization efficiency [8], the short diffusion length of minority carriers, and its sluggish surface catalytic reaction [9–11]. Therefore, detailed investigations on the optical–electrical conversion properties of TiO_2 are necessary to realize its promising water splitting ability.

Nowadays, the strategies to promote PEC performance mainly include heteroatom doping [12–14], deposited cocatalysts [11,15,16], and defect engineering. Heteroatom doping can positively affect the light harvesting property through modulating the band structure, but it fails to boost the surface oxidation reaction. In contrast, cocatalyst modification will enhance the surface catalytic reaction kinetics, but at the cost of reducing the light absorption efficiency of the semiconductor. Notably, defect engineering is capable of simultaneously optimizing the optical and electrical properties, resulting in enhanced light

harvesting, fast charge transportation, and suppressed bulk recombination. Meanwhile, the generated oxygen defects are reported to be capable of self-catalyzing water oxidation and decreasing the surface adsorption energy of water, thus boosting the catalytic reaction kinetics [17,18]. Nevertheless, excessive surface defects may act as the centers of charge recombination, inhibiting the separation of carriers on the surfaces of catalysts.

Polarization, including macroscopic polarization, piezoelectric polarization, ferroelectric polarization, and surface polarization, possesses the ability to promote the separation of photo-generated carriers via establishing a polarization electric field [19]. In particular, surface polarization that is obtained by introducing surface terminals (such as hydroxy groups and halogen ions) can drastically facilitate surface charge separation [20]. For instance, Ma and co-workers [21] recently reported a rational approach to building an efficient electric field via modifying the surface of TiO_2 with hydroxy groups, which promoted the water oxidation performance up to 1.41 mA cm^{-2} at 1.23 V_{RHE}. Despite this substantial progress, the PEC activity of TiO_2 is still not satisfactory. Developing a complementary method that can significantly improve the efficiency of TiO_2 photoanodes still remains a great challenge.

Herein, we demonstrate the preparation of TiO_{2-x} nanorod arrays by a simple $NaBH_4$ reduction treatment, which can simultaneously induce the generation of oxygen vacancies and hydroxy groups. Under PEC operation, the vacancies enable fast charge transport, enhanced charge injection, and accelerated surface catalytic kinetics. Meanwhile, the enriched hydroxy groups bring about a polarized electric field to promote surface charge migration and separation. Additionally, the ordered nanorod arrays facilitate electrolyte diffusion and provide a large accessible surface area for electrocatalytic active sites. As a consequence, the optimized TiO_{2-x} photoanode exhibits a highly enhanced photocurrent density of 2.62 mA cm^{-2} at 1.23 V_{RHE} in the absence of surface cocatalysts and hole scavengers, which is approximately two times higher than the pristine TiO_2. Moreover, the remarkably enhanced charge separation efficiency to 80% and charge injection efficiency to 97% at 1.23 V_{RHE} are accomplished. Our work demonstrates the possibility of using the synergistic effect of defect engineering and surface polarization in enhancing PEC water splitting performance, and this strategy can be extended to other solar utilization-related research areas.

2. Results and Discussion

Figure 1a schematically illustrates the synthesis procedures of the TiO_{2-x} photoanode. TiO_{2-x} NRs were firstly fabricated via a hydrothermal reduction process. As shown in Figures 1b and S1, densely aligned and tetragonal rutile TiO_2 nanorods with a single-crystalline structure were successfully grown on the FTO substrate. These nanorod bundles were composed of many tiny single TiO_2 crystals. After the $NaBH_4$ reduction, the radially grown TiO_2 NRs were well maintained (Figure 1d), indicating a negligible effect on the morphology. From the cross-section image (inset of Figure 1b,d), the nanorods were estimated to be ~2.5 μm in length and ~100 nm in diameter. From the TEM images, it can be seen that the TiO_{2-x} (Figure 1f) showed a defined nanorod with an average diameter of approximately 100 nm. The lattice spacing (Figure 1g) of 0.325 nm corresponded to the (110) crystal plane of the rutile TiO_2 phase [22]. Interestingly, the surface wettability of TiO_2 was greatly changed with reduced treatment, as evidenced by the decreased contact angle from 27.3° to 16° (Figure 1c,e). The enhanced hydrophilicity is of great benefit for the water absorption process, thus favoring PEC performance [23].

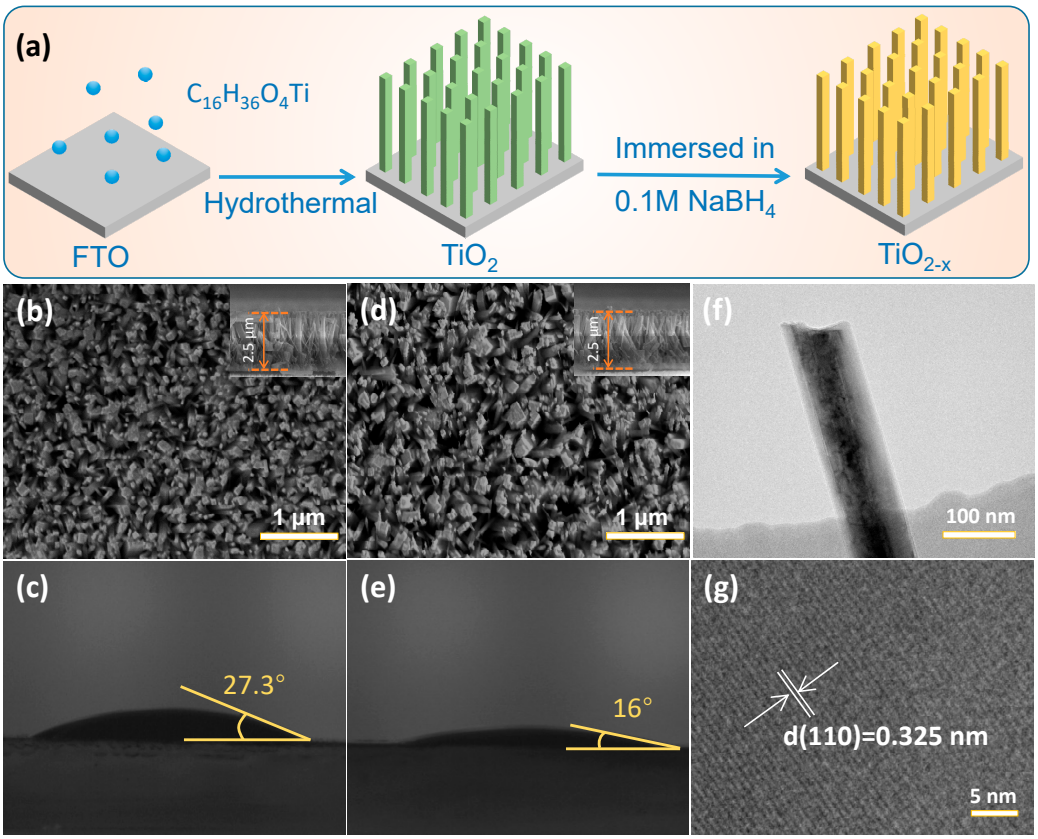


Figure 1. (**a**) Synthesis illustration of TiO_{2-x} photoanode; SEM of (**b**)TiO_2 and (**d**) TiO_{2-x}; (**f**) and (**g**) TEM images of TiO_{2-x}; contact angles of water droplets on (**c**) TiO_2 and (**e**) TiO_{2-x}.

The crystal structures of pristine TiO_2 and TiO_{2-x} were investigated by XRD. As displayed in Figure 2a, for the pristine TiO_2 NRs, the characteristic peaks located at 36°, 63°, and 70° were well indexed to the (101), (002), and (112) planes of tetragonal rutile TiO_2 (JCPDS No. 88-1175) [24]. To further determine the structure of the as-prepared samples, Raman spectroscopy was performed, and the results are presented in Figure 2b. The three Raman peaks appearing at 147, 447, and 607 cm^{-1} correspond to typical B_{1g}, E_g, and A_{1g} vibrational modes of rutile TiO_2, respectively. The broad band at 244 cm^{-1} is related to the multi-photon process of rutile TiO_2 [25–27]. It is worth noting that the intensity of all the Raman peaks for TiO_{2-x} is weaker than that of pristine TiO_2, arising from the reduced crystallinity induced by abundant oxygen vacancies [28,29].

XPS characterization was conducted to probe the surface chemical environment of TiO_{2-x}. As displayed in Figure 2c, the peaks centered at the binding energies (BE) of 458.4 and 464.2 eV are assigned to Ti $2p_{3/2}$ and Ti $2p_{1/2}$, respectively, coinciding with the Ti^{4+} values in the TiO_2 lattice [30–32]. After $NaBH_4$ reduction, the Ti 2p peaks are shifted to a lower BE in comparison to TiO_2, indicating the formation of Ti^{3+} [33]. The O 1s spectra (Figure 2d) of TiO_2 and TiO_{2-x} are all deconvoluted into four peaks centered at 529.8, 530.9, 531.5, and 532.1 eV, corresponding to the O^{2-} species in the lattice (O_L), oxygen vacancy (O_V), the hydroxyl oxygen (Ti-OH), and surface-absorbed water (O_A), respectively [11,34,35]. Accordingly, the relative content of these three O species (i.e., O_A, O_V, Ti-OH) was calculated and is shown in Figure 2e. It is important to note that the calculated O_V content in the TiO_{2-x} (8.9%) is much higher than that in the pristine TiO_2 (6.5%), suggesting the existence of abundant O_V. Meanwhile, the amount of hydroxyl oxygen also increased from 7.5% of TiO_2 to 11.9% of TiO_{2-x}. These enriched -OH groups with dipole moment can polarize the surface of TiO_2, leading to a drastic improvement in the charge separation efficiency [21,36]. To further characterize the O_V, EPR was carried out. As shown in Figure 2f, an obvious EPR signal at g = 2.001 appeared in TiO_{2-x}, which is the

typical signal of O_V, suggesting the existence of O_V in TiO_{2-x} [31,37]. It was encouraging that the intensity of the EPR signal for TiO_{2-x} was much stronger than that of the TiO_2 signal, indicating the enrichment of O_v in TiO_{2-x}, which was consistent with the XPS results (Figure 2d). The simultaneous existence of oxygen defects and hydroxy groups is expected to accelerate the charge separation, transport, and surface reaction activity.

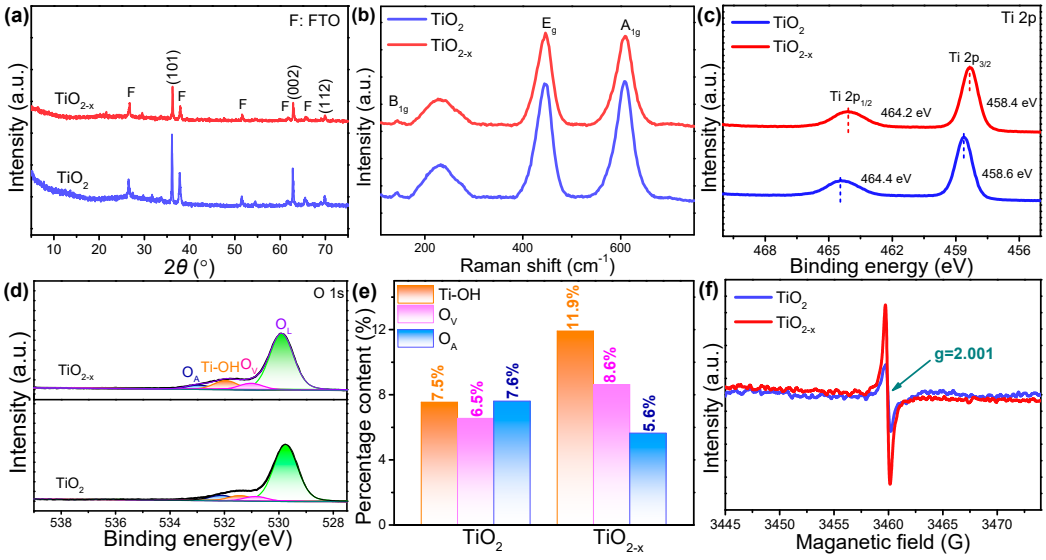


Figure 2. (**a**) XRD patterns and (**b**) Raman spectra of TiO_2 and TiO_{2-x}; XPS spectra of (**c**) Ti 2p, (**d**) O 1s of TiO_2 and TiO_{2-x}; (**e**) relative content of oxygen vacancy, Ti−OH, and adsorbed oxygen groups in the TiO_{2-x} photoanodes; (**f**) EPR curves of TiO_2 and TiO_{2-x}.

The PEC properties of the TiO_2 and TiO_{2-x} electrodes were monitored in a typical three-electrode system using 1 M NaOH as the electrolyte. The photocurrent densities of TiO_{2-x} with different $NaBH_4$ reduction times were compared to investigate the effect of the reduction degree on the PEC performance (Figure 3a). When TiO_2 was reduced by $NaBH_4$, the photocurrent density increased and surmounted at a reduction time of 40 min. Therefore, hereinafter, the discussion will focus on a comparison of the TiO_2 and TiO_{2-x} (40 min) to explore the underlying mechanism of the outstanding PEC performance of TiO_{2-x}. As shown in Figure 3b, the TiO_{2-x} exhibits a substantially increased photocurrent density of 2.6 mA cm^{-2}, which is approximately two times higher than that of pristine TiO_2. Encouragingly, such excellent performance of TiO_{2-x} surpasses that of most of the recently reported TiO_2-based photoelectrodes, such as TiO_2/NH_2-MIL($Fe_{0.25}Ni_{0.75}$)-88 (1.56 mA cm^{-2}) [38], Gly-TiO_2 (1.41 mA cm^{-2}) [21], Sn_3O_4/TiO_2/Au (2.5 mA cm^{-2}) [39], and MnO_2/N-TiO_2 NTs (1.95 mA cm^{-2}) [40] (Table S1). Moreover, the ABPE was calculated based on the LSV curves in Figure 3b. As shown in Figure 3c, for the TiO_{2-x} photoanode, the maximum ABPE value reaches 1.6% at 0.5 V_{RHE}, which is much higher than that of pristine TiO_2 (0.75% at 0.52 V_{RHE}). Additionally, the first derivatives of the photocurrent densities versus voltages, which can efficiently reflect the change rate of photocurrent density, are depicted in Figure 3d. Interestingly, the TiO_{2-x} demonstrates larger dJ/dV than TiO_2 at a low bias of <0.5 V_{RHE}, indicating that the charge transfer dynamics near the surface of the photoanode are expedited [41].

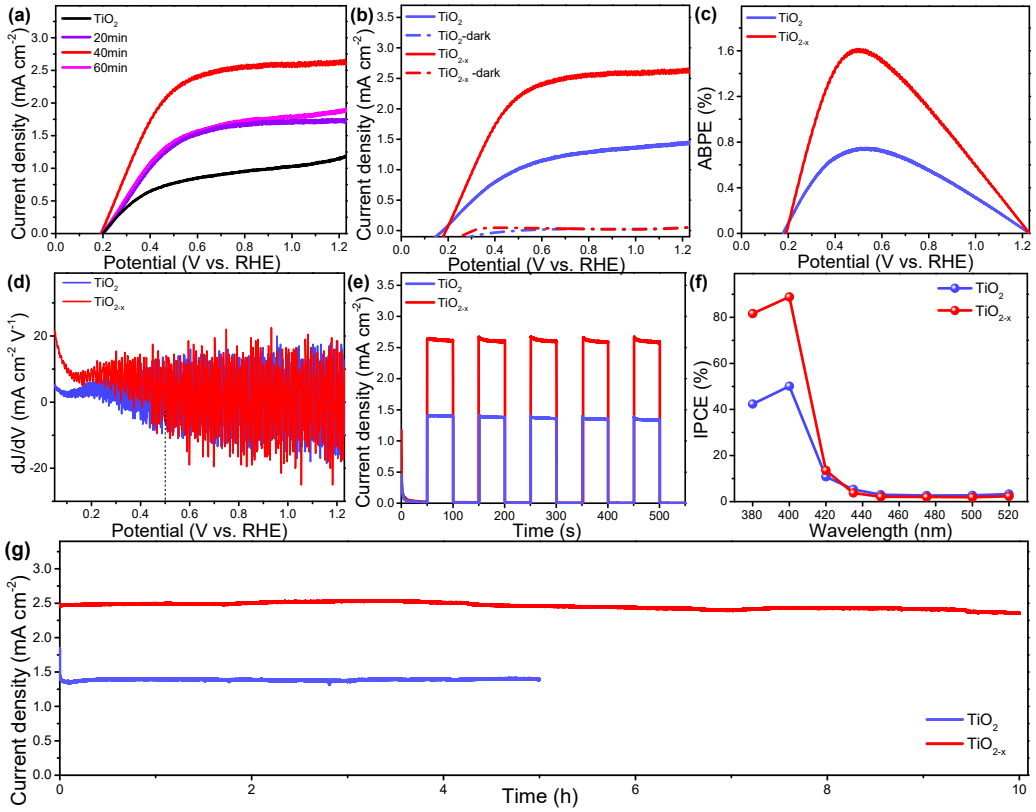


Figure 3. (**a**) LSV curves of TiO_{2-x} photoanodes with different $NaBH_4$ reduction times; (**b**) LSV curves; (**c**) ABPE values; (**d**) derivative curves of current with respect to voltage; (**e**) chopped current-time curves; (**f**) IPCE plots; (**g**) stability test at 1.23 V vs. RHE of TiO_2 and TiO_{2-x} photoanodes.

The transient photocurrent response curves (Figure 3e) were obtained via switching on/off the incident light for five consecutive cycles at 1.23 V_{RHE}, which demonstrates the same enhancement as that of the LSV curves. The gentle photocurrent spikes of the TiO_{2-x} suggest that the accumulation of photo-generated holes at the solid/liquid interface is inhibited thanks to the accelerated surface reaction kinetics [42]. To evaluate the photoactivity and light absorption of the catalysts, the IPCE was analyzed at 1.23 V_{RHE} (Figure 3f). The TiO_{2-x} photoanode displayed remarkably higher IPCE than bare TiO_2 in the light absorption range of 350-440 nm. It achieves a maximum IPCE value of 90% at approximately 400 nm, which is approximately 1.8 times that of TiO_2 (50%). The results indicate the efficient utilization of incident light (350–440 nm) for PEC water splitting. Furthermore, the durability of TiO_{2-x} and TiO_2 was measured at 1.23 V_{RHE} under continuous illumination for 10 h (Figure 3g). The TiO_{2-x} exhibited a high photocurrent density of around 2.5 mA cm^{-2} without obvious degradation, demonstrating its excellent electrochemically stable property during the PEC water splitting process.

The PEC performance of a photoanode is theoretically related to the light harvesting efficiency ($\eta_{absorbance}$), charge injection efficiency ($\eta_{injection}$), and separation efficiency ($\eta_{separation}$). Thereby, to explore the underlying mechanism of the excellent performance of TiO_{2-x}, we systematically studied the optical property and charge behavior of TiO_{2-x}. Firstly, the optical properties of TiO_{2-x} and TiO_2 were characterized with UV-vis diffuse reflection spectra (DRS). As shown in Figure 4a, the absorbance edge of TiO_{2-x} shows a negligible shift compared with that of TiO_2. Meanwhile, the bandgaps of TiO_{2-x} derived from the DRS spectra based on the Kubelka-Munk equation also reveal little difference with TiO_2 (the inset of Figure 4a), indicative that the $\eta_{absorbance}$ is not the main reason for the enhanced PEC activity.

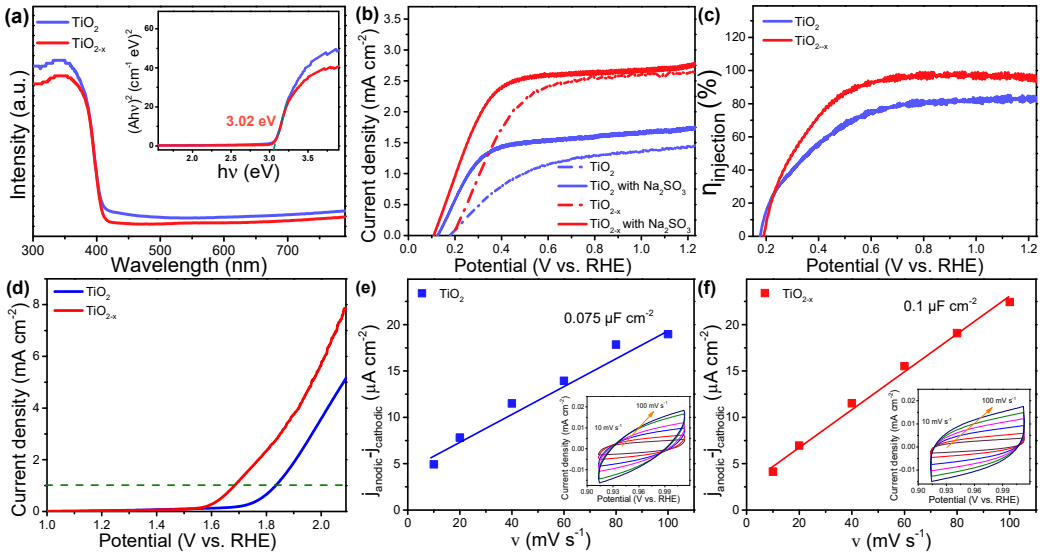


Figure 4. (**a**) UV-vis diffuse reflectance spectra; the inset shows the Tauc plots of TiO_2 and TiO_{2-x}; (**b**) LSV curves of TiO_2 and TiO_{2-x} photoanodes in the presence of sacrifice agents (0.5 M Na_2SO_3); (**c**) charge injection efficiencies; (**d**) LSV curves in dark of TiO_2 and TiO_{2-x}; relative electrochemical surface areas (ECSA) of (**e**) TiO_2 and (**f**) TiO_{2-x}; linear relationship between the capacitive current and scan rate; the insets show the CV curves of TiO_2 and TiO_{2-x} under different scan rates, respectively.

Then, the $\eta_{injection}$ was quantified using the LSV data measured in 1.0 M NaOH electrolyte containing 0.5 M Na_2SO_3 (Figure 4b). Since sulfite oxidation is a very fast process, assuming that all the photogenerated holes can be immediately consumed once they reach the surface [43], the $\eta_{injection}$ with Na_2SO_3 can be regarded as 100%. The charge injection efficiency ($\eta_{injection}$) can be calculated by the equation of $\eta_{injection}$ (%) = $J_{H2O}/J_{Na2SO3} \times 100$, in which J_{H2O} and J_{Na2SO3} are the photocurrent density without and with Na_2SO_3 as hole scavengers, respectively. As shown in Figure 4c, the $\eta_{injection}$ of TiO_{2-x} is sharply increased to 97% in comparison to that of TiO_2 (80%) at 1.23 V_{RHE}, implying that the TiO_{2-x} photoanode possesses superior intrinsic electrocatalytic activity for water oxidation, which was further validated by the oxygen evolution reaction performance (Figure 4d). To drive the current density of 1 mA cm^{-2}, TiO_{2-x} requires an overpotential of 450 mV, which is approximately 150 mV lower than that of TiO_2. Furthermore, from the anodic/cathodic current densities in the CV curves measured under different scan rates (insets of Figure 4e,f), we could calculate the relative electrochemical surface areas (ECSA) of TiO_2 and TiO_{2-x}. The electrochemically active area of TiO_{2-x} was clearly much higher than that of TiO_2. This is consistent with the higher $\eta_{injection}$ value of TiO_{2-x}. The faster charge injection efficiency and improved number of active sites could be related to the abundant oxygen defects in TiO_{2-x} caused by $NaBH_4$ reduction, contributing to the enhanced PEC performance.

Finally, the charge separation efficiency ($\eta_{separation}$) was calculated using the formula of $\eta_{separation}$ (%) = $J_{Na2SO3}/J_{abs} \times 100$, where J_{abs} can be obtained by assuming that all the photons absorbed by the semiconductor are converted into a current. As shown in Figure 5a, TiO_{2-x} achieves a $\eta_{separation}$ of approximately 80% at 1.23 V_{RHE}, which is ~two times higher than that of TiO_2. The improved charge separation is also verified by the PL spectra in Figure 5b. The PL intensity of TiO_{2-x} is weaker than that of TiO_2 throughout the measured wavelength, demonstrating the efficient separation of electron-hole pairs [44,45]. An EIS test was carried out to study the charge transfer kinetics. The Nyquist plots were analyzed by the equivalent circuit model (inset), in which R_s, R_{ct1}, and R_{ct2} correspond to the external circuit resistance, charge transport resistance of the photoanode, and electron transfer resistance of the PEC reaction at the solid electrode/electrolyte interface [46]. The

obtained fitting parameters are shown in Table S2. Notably, the TiO_{2-x} exhibited lower R_s, R_{ct1}, and R_{ct2} values than the TiO_2, indicating enhanced charge transfer efficiency.

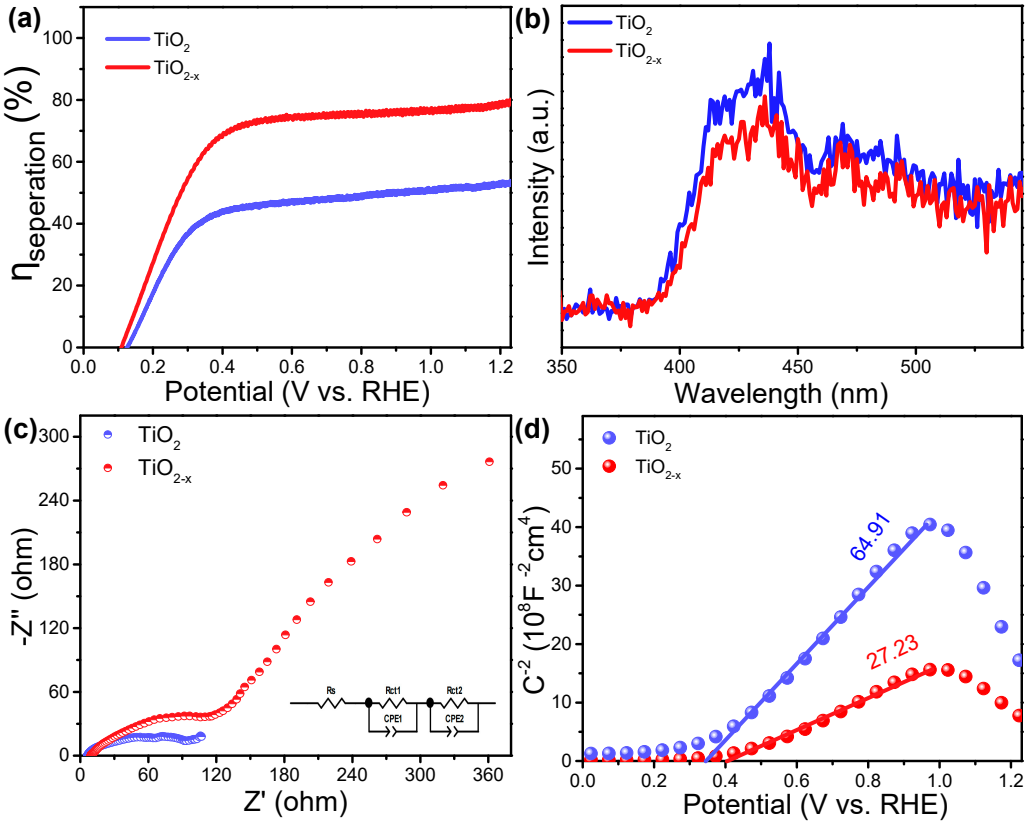


Figure 5. (**a**) Bulk charge separation efficiency; (**b**) PL plots; (**c**) Nyquist plots measured at open circuit; (**d**) M-S plots under dark of TiO_2 and TiO_{2-x}.

Additionally, the M-S plots were obtained under dark conditions to further clarify the charge transfer behavior of the two samples. As presented in Figure 5d, the positive slopes of both curves suggest that the n-type semiconductor essence of TiO_2 is not changed by $NaBH_4$ reduction [47]. Meanwhile, TiO_{2-x} displays smaller slopes than TiO_2, suggesting that reduction increases the carrier concentration. The carrier concentration (N_d) can be calculated according to the equation of $N_d = [2/(e_0 \varepsilon \varepsilon_0)] [d(1/C^2)/dE]^{-1}$, where e_0, ε, ε_0, and E correspond to the elemental charge (1.6×10^{-19} C), dielectric constant of rutile TiO_2, permittivity of vacuum, and applied electrode potential. The calculated result of TiO_{2-x} is 1.48×10^{19} cm^{-3}, which is 2.4 times larger than that of the pristine TiO_2 (6.21×10^{18} cm^{-3}). The increased carrier concentration can be attributed to the existence of oxygen vacancies, which can enhance the bulk electrical conductivity of TiO_2. It is worth noting that the flat band potential of TiO_{2-x} experiences a positive shift, which can be attributed to the polarized surface induced by hydroxyl groups. This polarization builds a polarized electric field near the surface, facilitating charge transfer to the surface for the catalytic reaction [20,48,49].

Based on the above results, a rational mechanism for the enhanced PEC performance of TiO_{2-x} is proposed in Figure 6. Upon light illumination, the photo-generated holes rapidly migrate to the photoanode surface thanks to the enhanced conductivity and the formation of a surface-polarized electric field, which could increase the driving force to facilitate charge separation and transport. Moreover, the oxygen vacancies on the surface could act as the active sites for the water oxidation reaction. Meanwhile, the separated electrons located in TiO_2 migrate to the counter electrode for the reduction reaction. Thus, the coexistence of oxygen vacancies and hydroxy groups in TiO_{2-x} not only efficiently suppresses surface and bulk charge recombination, but also supplies the active sites for the catalytic reaction.

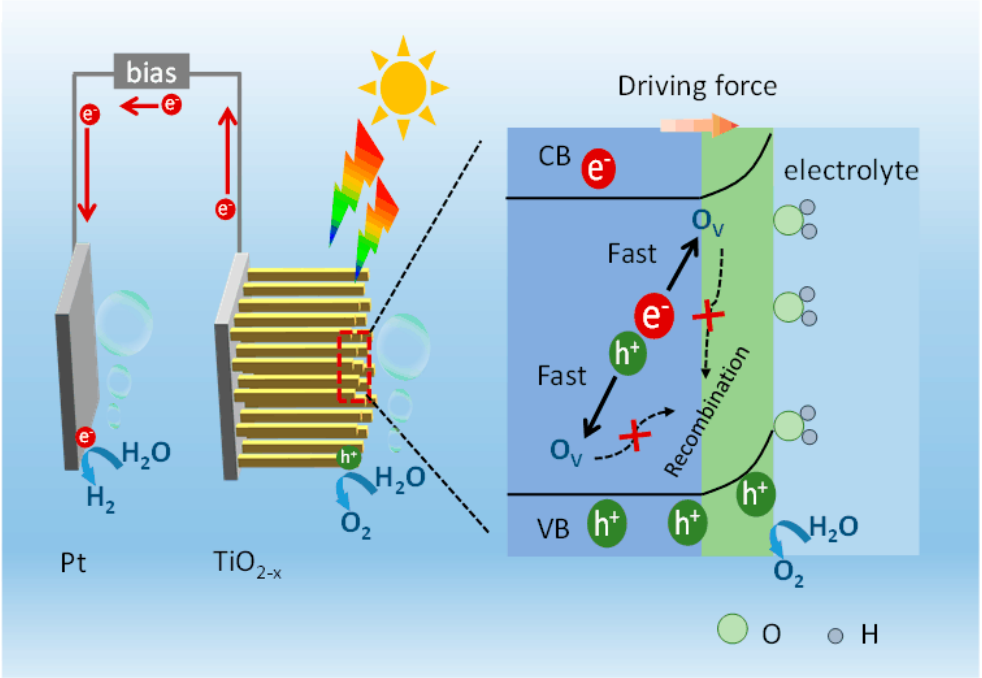


Figure 6. Schematic representation of PEC water oxidation mechanism on TiO_{2-x} photoelectrode.

3. Conclusions

In conclusion, a TiO_{2-x} photoanode with an ordered nanorod array architecture has been successfully fabricated by an in situ chemical reduction method. Thanks to the coexistence of oxygen vacancies and hydroxy groups, the as-obtained TiO_{2-x} photoanode enables a significant enhancement in the PEC performance by accelerating the charge transport/separation and surface reaction kinetics. A highly increased photocurrent density of 2.6 mA cm^{-2} with outstanding durability is achieved at the potential of 1.23 V versus RHE. It is believed that the present work will provide an innovative design and pave the way towards introducing oxygen vacancies for various semiconductors in PEC systems.

4. Materials and Methods

4.1. Materials Synthesis

The TiO_2 nanorod arrays (TiO_2 NRs) were synthesized by a hydrothermal process. Typically, 0.4 mL of tetrabutyl titanate was added to 24 mL HCl aqueous solution (12 mL of deionized water and 12 mL of hydrochloric acid) and stirred for 30 min. Then, the mixture was transferred into a 50 mL Teflon-lined autoclave with a piece of FTO substrate. The sealed autoclave was placed in an oven at 180 °C for 8 h. Afterward, the cooled TiO_2 NRs were rinsed with DI water. Finally, the TiO_2 NRs were placed in a muffle furnace and calcined at 450 °C for 2 h in air, and then left to cool naturally to increase the crystallinity of the TiO_2 nanorod arrays.

The as-prepared TiO_2 NRs were immersed in 0.1 M of $NaBH_4$ for 40 min at room temperature, followed by rinsing with DI water and drying in N_2 flow. The obtained sample is referred to as TiO_{2-x}.

4.2. Material Characterization

The morphology and composition were examined by field emission scanning electron microscopy (SEM, FEI Nano SEM 450) and transmission electronic microscopy (TEM, FEI Talos F200X). The crystalline structure was characterized by X-ray diffraction (XRD, Bruker D8, Karlsruhe, Germany) with a Cu Kα (λ = 0.15406 nm) source. The light absorption spectra were recorded with a UV-vis spectrophotometer, with high-purity $BaSO_4$ as a reference (UH4150). The surface elemental compositions and states were analyzed by

X-ray photoelectron spectroscopy (XPS, Kratons AXIS Ultra DLD) with an Al Kα source (hν = 1486.6 eV). The electron paramagnetic resonance (EPR) measurements were recorded using a JES-FA200 spectrometer at room temperature. Photoluminescence (PL) intensity was measured by a fluorescence spectrometer (FLS980) at room temperature.

4.3. Photoelectrochemical Measurements

All of the photoelectrochemical measurements were performed on a CHI760E electrochemical workstation via a typical three-electrode system. In a typical test system, the as-prepared TiO_{2-x} photoanode (1 cm^2 working area), Pt plate (1 cm × 1 cm), and Ag/AgCl (saturated KCl) were employed as the working electrodes, counter electrode, and reference electrode, respectively, as shown in Figure S2. Moreover, 1 M NaOH (pH = 13.7) was used as the electrolyte. A 300 W Xe lamp was chosen to provide a light source, with an incident light intensity of 100 mW cm^{-2}. The typical linear sweep voltammetry (LSV) curves were measured under a scan rate of 10 mV s^{-1} in the forward direction. The applied potential vs. Ag/AgCl was converted to the reference hydrogen electrode (RHE) using the following equation [24]: $E_{RHE} = E_{Ag/AgCl} + E^0{}_{Ag/AgCl} + 0.0591 \times pH$ ($E^0{}_{Ag/AgCl}$ = 0.1976 V vs. NHE at 25 °C), where E_{RHE} and $E_{Ag/AgCl}$ refer to the potentials vs. RHE and experimentally applied potential. The electrochemical impedance spectroscopy (EIS) was measured at the open-circuit voltage under illumination, sweeping in the frequency range from 10^5 Hz to 10^{-2} Hz. The applied bias photon-to-current efficiency (ABPE) of the electrodes could be quantized by the photocurrent densities at different potentials using the formula below [50]:

$$ABPE(\%) = J_{ph} \times (1.23 - V_{bias})/Pin \times 100 \quad (1)$$

where J_{ph}, $V_{bias,}$ and P_{in} are the current density (mA cm^{-2}) obtained from the LSV curve, applied potential (V vs. RHE), and the power density of incident light (mW cm^{-2}), respectively.

The incident photon-to-current conversion efficiency (IPCE) of the samples was calculated on the basis of the following equation:

$$IPCE(\%) = 1240 \times J_{ph} / Pin \times \lambda \times 100 \quad (2)$$

where J_{ph} refers to the current density (mA cm^{-2}) at a certain wavelength, P_{in} is the power density of the incident light at the corresponding wavelength, and λ represents the wavelength of the corresponding incident light.

Supplementary Materials: The following supporting information can be downloaded at: https://www.mdpi.com/article/10.3390/catal12091021/s1. Figure S1: (a) HRTEM and (b) SAED pattern of TiO_2; Figure S2: Digital images of (a) the electrochemical cell and (b) as-prepared TiO_2 and TiO_{2-x} samples; Table S1: Comparison of PEC performance for TiO_2-based photoelectrodes [11,21,33,38–40,50–58]; Table S2: The fitted values of Nyquist plots according to the equivalent circuit in Figure 5c.

Author Contributions: Y.L. and S.L.: writing—original draft preparation; J.-G.W. and Y.L.: conceptualization, supervision, funding, writing—review and editing; H.S. and W.H.: investigation, resources. All authors have read and agreed to the published version of the manuscript.

Funding: This work is financially supported by the National Natural Science Foundation of China (52272239), Fundamental Research Program of Qinghai Province (2021-ZJ-941Q), Youth Research Foundation Project of Qinghai University (2020-QGY-5) and Fundamental Research Funds for the Central Universities (D5000210894).

Data Availability Statement: Not applicable.

Acknowledgments: The authors appreciate the support of the Analytical & Testing Center of Northwestern Polytechnical University during the TEM analysis.

Conflicts of Interest: The authors declare no conflict of interest.

References

1. Gong, J.; Li, C.; Wasielewski, M.R. Advances in solar energy conversion. *Chem. Soc. Rev.* **2019**, *48*, 1862–1864. [CrossRef]
2. Chen, X.; Shen, S.; Guo, L.; Mao, S.S. Semiconductor-based Photocatalytic Hydrogen Generation. *Chem. Rev.* **2010**, *110*, 6503–6570. [CrossRef] [PubMed]
3. Mao, S.S.; Shen, S. Catalysing artificial photosynthesis. *Nat. Photonics* **2013**, *7*, 944–946. [CrossRef]
4. Osterloh, F.E. Inorganic nanostructures for photoelectrochemical and photocatalytic water splittin. *Chem. Soc. Rev.* **2013**, *42*, 2294–2320. [CrossRef] [PubMed]
5. Nath, N.C.D.; Viswanathan, P.; Yadav, H.M.; Yoo, K.; Kang, H.C.; Lee, J.-J. Stand-Alone Photoelectrochemical Energy Conversions. *Solar RRL* **2021**, *5*, 2000517. [CrossRef]
6. Liu, H.; Wang, J.-G.; Hua, W.; Ren, L.; Sun, H.; Hou, Z.; Huyan, Y.; Cao, Y.; Wei, C.; Kang, F. Navigating fast and uniform zinc deposition via a versatile metal-organic complex interphase. *Energy Environ. Sci.* **2022**, *15*, 1872–1881. [CrossRef]
7. Yadav, H.M.; Thorat, N.D.; Yallapu, M.M.; Tofail, S.A.M.; Kim, J.S. Functional TiO_2 nanocoral architecture for light-activated cancer chemotherapy. *J. Mater. Chem. B* **2017**, *5*, 1461–1470. [CrossRef]
8. Khan Shahed, U.M.; Al-Shahry, M.; Ingler William, B. Efficient Photochemical Water Splitting by a Chemically Modified n-TiO_2. *Science* **2002**, *297*, 2243–2245. [CrossRef] [PubMed]
9. Butburee, T.; Bai, Y.; Wang, H.; Chen, H.; Wang, Z.; Liu, G.; Zou, J.; Khemthong, P.; Lu, G.Q.M.; Wang, L. 2D Porous TiO_2 Single-Crystalline Nanostructure Demonstrating High Photo-Electrochemical Water Splitting Performance. *Adv. Mater.* **2018**, *30*, 1705666. [CrossRef]
10. Li, X.; Xiong, J.; Xu, Y.; Feng, Z.; Huang, J. Defect-assisted surface modification enhances the visible light photocatalytic performance of g-C_3N_4@C-TiO_2 direct Z-scheme heterojunctions. *Chin. J. Catal.* **2019**, *40*, 424–433. [CrossRef]
11. Pal, D.; Sarkar, A.; Ghosh, N.G.; Sanke, D.M.; Maity, D.; Karmakar, K.; Sarkar, D.; Zade, S.S.; Khan, G.G. Integration of $LaCo(OH)_x$ photo-electrocatalyst and plasmonic gold nanoparticles with Sb-doped TiO_2 Nanorods for photoelectrochemical water oxidation. *ACS Appl. Nano Mater.* **2021**, *4*, 6111–6123. [CrossRef]
12. Xie, Z.; Zhang, Y.; Liu, X.; Wang, W.; Zhan, P.; Li, Z.; Zhang, Z. Visible Light Photoelectrochemical Properties of N-Doped TiO_2 Nanorod Arrays from TiN. *J. Nanomater.* **2013**, *2013*, 1–8.
13. Cheng, C.; Sun, Y. Carbon doped TiO_2 nanowire arrays with improved photoelectrochemical water splitting performance. *Appl. Surf. Sci.* **2012**, *263*, 273–276. [CrossRef]
14. Lu, R.; Wei, Y.; Chen, C.; Wu, T. Visible-light-driven photoelectrochemical water oxidation with Al doped TiO_2 nanorod arrays. *J. Alloy. Compd.* **2019**, *790*, 99–108. [CrossRef]
15. Ren, X.; Ji, Y.; Zhai, Y.; Yuan, N.; Ding, J.; Li, Y.; Yan, J.; Liu, S.F. Self-assembled CoOOH on TiO_2 for enhanced photoelectrochemical water oxidation. *J. Energy Chem.* **2021**, *60*, 512–521. [CrossRef]
16. Khnayzer, R.S.; Mara, M.W.; Huang, J.; Shelby, M.L.; Chen, L.X.; Castellano, F.N. Structure and Activity of Photochemically Deposited "CoPi" Oxygen Evolving Catalyst on Titania. *ACS Catal.* **2012**, *2*, 2150–2160. [CrossRef]
17. Rahman, M.A.; Bazargan, S.; Srivastava, S.; Wang, X.; Abd-Ellah, M.; Thomas, J.P.; Heinig, N.F.; Pradhan, D.; Leung, K.T. Defect-rich decorated TiO_2 nanowires for super-efficient photoelectrochemical water splitting driven by visible light. *Energy Environ. Sci.* **2015**, *8*, 3363–3373. [CrossRef]
18. Liang, J.; Wang, N.; Zhang, Q.; Liu, B.; Kong, X.; Wei, C.; Zhang, D.; Yan, B.; Zhao, Y.; Zhang, X. Exploring the mechanism of a pure and amorphous black-blue TiO_2:H thin film as a photoanode in water splitting. *Nano Energy* **2017**, *42*, 151–156. [CrossRef]
19. Chen, F.; Huang, H.; Guo, L.; Zhang, Y.; Ma, T. The Role of Polarization in Photocatalysis. *Angew. Chem. Int. Ed.* **2019**, *58*, 10061–10073. [CrossRef] [PubMed]
20. Hao, L.; Kang, L.; Huang, H.; Ye, L.; Han, K.; Yang, S.; Yu, H.; Batmunkh, M.; Zhang, Y.; Ma, T. Surface-Halogenation-Induced Atomic-Site Activation and Local Charge Separation for Superb CO_2 Photoreduction. *Adv. Mater.* **2019**, *31*, 1900546. [CrossRef]
21. Ma, W.; Huang, K.; Wu, X.; Wang, M.; Feng, S. Surface polarization enables high charge separation in TiO_2 nanorod photoanode. *Nano Res.* **2021**, *14*, 4056–4062. [CrossRef]
22. Hosono, E.; Fujihara, S.; Kakiuchi, K.; Imai, H. Growth of Submicrometer-Scale Rectangular Parallelepiped Rutile TiO_2 Films-in Aqueous $TiCl_3$ Solutions under Hydrothermal Conditions. *J. Am. Chem. Soc.* **2004**, *126*, 7790–7791. [CrossRef] [PubMed]
23. Li, J.; Gao, X.; Li, Z.; Wang, J.H.; Zhu, L.; Yin, C.; Wang, Y.; Li, X.B.; Liu, Z.; Zhang, J.; et al. Superhydrophilic Graphdiyne Accelerates Interfacial Mass/Electron Transportation to Boost Electrocatalytic and Photoelectrocatalytic Water Oxidation Activity. *Adv. Funct. Mater.* **2019**, *29*, 1808079. [CrossRef]
24. Wu, F.; Yu, Y.; Yang, H.; German, L.N.; Li, Z.; Chen, J.; Yang, W.; Huang, L.; Shi, W.; Wang, L.; et al. Simultaneous Enhancement of Charge Separation and Hole Transportation in a TiO_2-$SrTiO_3$ Core-Shell Nanowire Photoelectrochemical System. *Adv. Mater.* **2017**, *29*, 1701432. [CrossRef] [PubMed]
25. Xia, X.; Peng, S.; Bao, Y.; Wang, Y.; Lei, B.; Wang, Z.; Huang, Z.; Gao, Y. Control of interface between anatase TiO_2 nanoparticles and rutile TiO_2 nanorods for efficient photocatalytic H_2 generation. *J. Power Sources* **2018**, *376*, 11–17. [CrossRef]
26. Balachandran, U.; Eror, N.G. Raman spectra of titanium dioxide. *J. Solid State Chem.* **1982**, *42*, 276–282. [CrossRef]
27. Choi, H.C.; Jung, Y.M.; Kim, S.B. Size effects in the Raman spectra of TiO_2 nanoparticles. *Vib. Spectrosc.* **2005**, *37*, 33–38. [CrossRef]
28. Wang, G.; Ling, Y.; Lu, X.; Qian, F.; Tong, Y.; Zhang, J.Z.; Lordi, V.; Rocha Leao, C.; Li, Y. Computational and Photoelectrochemical Study of Hydrogenated Bismuth Vanadate. *J. Phys. Chem. C* **2013**, *117*, 10957–10964. [CrossRef]

29. Wang, S.; Chen, P.; Yun, J.H.; Hu, Y.; Wang, L. An Electrochemically Treated $BiVO_4$ Photoanode for Efficient Photoelectrochemical Water Splitting. *Angew. Chem. Int.* **2017**, *56*, 8500–8504. [CrossRef]
30. Li, Y.Y.; Wang, J.G.; Sun, H.H.; Wei, B. Heterostructured $TiO_2/NiTiO_3$ nanorod arrays for inorganic sensitized solar cells with significantly enhanced photovoltaic performance and stability. *ACS Appl. Mater. Interfaces* **2018**, *10*, 11580–11586. [CrossRef]
31. Zheng, L.; Ye, X.; Deng, X.; Wang, Y.; Zhao, Y.; Shi, X.; Zheng, H. Black Phosphorus Quantum Dot-Sensitized TiO_2 Nanotube Arrays with Enriched Oxygen Vacancies for Efficient Photoelectrochemical Water Splitting. *ACS Sustain. Chem. Eng.* **2020**, *8*, 15906–15914. [CrossRef]
32. Zhou, B.X.; Ding, S.S.; Wang, Y.; Wang, X.R.; Huang, W.Q.; Li, K.; Huang, G.F. Type-II/type-II band alignment to boost spatial charge separation: A case study of g-C_3N_4 quantum dots/a-TiO_2/r-TiO_2 for highly efficient photocatalytic hydrogen and oxygen evolution. *Nanoscale* **2020**, *12*, 6037–6046. [CrossRef] [PubMed]
33. Kang, Q.; Cao, J.; Zhang, Y.; Liu, L.; Xu, H.; Ye, J. Reduced TiO_2 nanotube arrays for photoelectrochemical water splitting. *J. Mater. Chem. A* **2013**, *1*, 5766–5774. [CrossRef]
34. Li, L.; Zhang, G.; Wang, B.; Yang, S. Constructing the Fe/Cr double (oxy)hydroxides on Fe_3O_4 for boosting the electrochemical oxygen evolution in alkaline seawater and domestic sewage. *Appl. Catal. B Environ.* **2022**, *302*, 120847. [CrossRef]
35. Liu, Q.-Y.; Wang, H.-D.; Tang, R.; Cheng, Q.; Yuan, Y.-J. Rutile TiO_2 nanoparticles with oxygen vacancy for photocatalytic nitrogen fixation. *ACS Appl. Nano Mater.* **2021**, *4*, 8674–8679. [CrossRef]
36. Zhang, R.; Bi, L.; Wang, D.; Lin, Y.; Zou, X.; Xie, T. An effective method to understand photo-generated charge transfer processes of Z-scheme Ti/α-Fe2O_3/g-C_3N_4 photocatalysts for hydrogen evolution. *Catal. Commun.* **2020**, *142*, 106028. [CrossRef]
37. Zhang, H.; Cai, J.; Wang, Y.; Wu, M.; Meng, M.; Tian, Y.; Li, X.; Zhang, J.; Zheng, L.; Jiang, Z.; et al. Insights into the effects of surface/bulk defects on photocatalytic hydrogen evolution over TiO_2 with exposed {001} facets. *Appl. Catal. B Environ.* **2018**, *220*, 126–136. [CrossRef]
38. Yoon, J.W.; Kim, J.-H.; Jo, Y.-M.; Lee, J.-H. Heterojunction between bimetallic metal-organic framework and TiO_2: Band-structure engineering for effective photoelectrochemical water splitting. *Nano Research* **2022**, *15*, 8502–8509. [CrossRef]
39. Dong, G.; Cheng, X.; Bi, Y. Hierarchical TiO_2 photoanodes with spatial charge separation for efficient oxygen evolution reaction. *Solar RRL* **2020**, *5*, 2000449. [CrossRef]
40. Cheng, X.; Dong, G.; Zhang, Y.; Feng, C.; Bi, Y. Dual-bonding interactions between MnO_2 cocatalyst and TiO_2 photoanodes for efficient solar water splitting. *Appl. Catal. B Environ.* **2020**, *267*, 118723. [CrossRef]
41. Xiao, J.; Zhao, F.; Zhong, J.; Huang, Z.; Fan, L.; Peng, L.; Zhou, S.-F.; Zhan, G. Performance enhancement of hematite photoanode with oxygen defects for water splitting. *Chem. Eng. J.* **2020**, *402*, 126163. [CrossRef]
42. Sun, H.; Hua, W.; Li, Y.; Wang, J.-G. Conformal coating of superhydrophilic metal-organic complex toward substantially improved photoelectrochemical water oxidation. *Chem. Eng. J.* **2022**, *427*, 131004. [CrossRef]
43. Kim Tae, W.; Choi, K.-S. Nanoporous $BiVO_4$ photoanodes with Dual-Layer oxygen evolution catalysts for solar water splitting. *Science* **2014**, *343*, 990–994. [CrossRef] [PubMed]
44. Zhang, H.; Ma, L.; Ming, J.; Liu, B.; Zhao, Y.; Hou, Y.; Ding, Z.; Xu, C.; Zhang, Z.; Long, J. Amorphous $Ta_2O_xN_y$-enwrapped TiO_2 rutile nanorods for enhanced solar photoelectrochemical water splitting. *Appl. Catal. B Environ.* **2019**, *243*, 481–489. [CrossRef]
45. Zhang, X.; Guo, H.; Dong, G.; Zhang, Y.; Lu, G.; Bi, Y. Homostructural Ta_3N_5 nanotube/nanoparticle photoanodes for highly efficient solar-driven water splitting. *Appl. Catal. B Environ.* **2020**, *277*, 119217. [CrossRef]
46. Li, Y.; Wang, J.-G.; Fan, Y.; Sun, H.; Hua, W.; Liu, H.; Wei, B. Plasmonic TiN boosting nitrogen-doped TiO_2 for ultrahigh efficient photoelectrochemical oxygen evolution. *Appl. Catal. B Environ.* **2019**, *246*, 21–29. [CrossRef]
47. Zhou, B.X.; Ding, S.S.; Zhang, B.J.; Xu, L.; Chen, R.S.; Luo, L.; Huang, W.Q.; Xie, Z.; Pan, A.; Huang, G.F. Dimensional transformation and morphological control of graphitic carbon nitride from water-based supramolecular assembly for photocatalytic hydrogen evolution: From 3D to 2D and 1D nanostructures. *Appl. Catal. B Environ.* **2019**, *254*, 321–328. [CrossRef]
48. Bae, S.; Kim, D.; Kim, H.; Gu, M.; Ryu, J.; Kim, B.S. Modulating Charge Separation Efficiency of Water Oxidation Photoanodes with Polyelectrolyte-Assembled Interfacial Dipole Layers. *Adv. Funct. Mater.* **2019**, *30*, 1908492. [CrossRef]
49. Zhang, B.; Chou, L.; Bi, Y. Tuning surface electronegativity of $BiVO_4$ photoanodes toward high-performance water splitting. *Appl. Catal. B Environ.* **2020**, *262*, 118267. [CrossRef]
50. Zhou, T.; Li, L.; Li, J.; Wang, J.; Bai, J.; Xia, L.; Xu, Q.; Zhou, B. Electrochemically reduced TiO_2 photoanode coupled with oxygen vacancy-rich carbon quantum dots for synergistically improving photoelectrochemical performance. *Chem. Eng. J.* **2021**, *425*, 131770. [CrossRef]
51. Wang, X.; Sun, W.; Tian, Y.; Dang, K.; Zhang, Q.; Shen, Z.; Zhan, S. Conjugated pi electrons of MOFs drive charge separation at heterostructures interface for enhanced photoelectrochemical water oxidation. *Small* **2021**, *17*, 2100367. [CrossRef] [PubMed]
52. Pang, Y.; Zang, W.; Kou, Z.; Zhang, L.; Xu, G.; Lv, J.; Gao, X.; Pan, Z.; Wang, J.; Wu, Y. Assembling of Bi atoms on TiO_2 nanorods boosts photoelectrochemical water splitting of semiconductors. *Nanoscale* **2020**, *12*, 4302–4308. [CrossRef] [PubMed]
53. He, Y.; Zhu, J.; Yuan, Y.; Li, M.; Yang, Y.; Liu, Y.; Chen, M.; Cao, D.; Yan, X. Dual-regulation charge separation strategy with the synergistic effect of 1D/0D heterostructure and inserted ferroelectric layer for boosting photoelectrochemical water oxidation. *J. Mater. Chem. A* **2021**, *9*, 7594–7605. [CrossRef]
54. Cui, W.; Bai, H.; Shang, J.; Wang, F.; Xu, D.; Ding, J.; Fan, W.; Shi, W. Organic-inorganic hybrid-photoanode built from NiFe-MOF and TiO_2 for efficient PEC water splitting. *Electrochim. Acta* **2020**, *349*, 136383. [CrossRef]

55. Wang, L.; Si, W.; Ye, Y.; Wang, S.; Hou, F.; Hou, X.; Cai, H.; Dou, S.X.; Liang, J. Cu-Ion-Implanted and Polymeric Carbon Nitride-Decorated TiO_2 Nanotube Array for Unassisted Photoelectrochemical Water Splitting. *ACS Appl. Mater. Interfaces* **2021**, *13*, 44184–44194. [CrossRef]
56. Zhang, S.; Liu, Z.; Chen, D.; Guo, Z.; Ruan, M. Oxygen vacancies engineering in TiO_2 homojunction/ZnFe-LDH for enhanced photoelectrochemical water oxidation. *Chem. Eng. J.* **2020**, *395*, 125101. [CrossRef]
57. Huang, C.; Bian, J.; Guo, Y.; Huang, M.; Zhang, R.-Q. Thermal vacuum de-oxygenation and post oxidation of TiO_2 nanorod arrays for enhanced photoelectrochemical properties. *J. Mater. Chem. A* **2019**, *7*, 5434–5441. [CrossRef]
58. Dong, Z.; Cai, Y.; Zhang, K.; Chu, Z.; Han, S.; Li, Z. Electrochemical reduction induced self-doping of oxygen vacancies into Ti–Si–O nanotubes as efficient photoanode for boosted photoelectrochemical water splitting. *Int. J. Hydrogen Energy* **2021**, *46*, 3554–3564. [CrossRef]